

1 **Model Description** *modified from:*

2 Liu, X^{†*} and **NM Levine**[†], Ecosystem implications of fine-scale physical disturbance in the oligotrophic ocean (2021),
 3 *Progress in Oceanography*, doi.org/10.1016/j.pocean.2021.102519
 4

5 **Physical model description**

6 The primary goal of this study was to assess the impact of fine-scale biophysical interactions
 7 on ecosystem and carbon cycling dynamics. To accomplish this, we used a zero-dimensional, mixed
 8 layer model to simulate large-scale interannual and seasonal dynamics at a study site (Fig. 1). Hereafter,
 9 we refer to the large-scale dynamics as the *background state*. We then layered fine-scale dynamics on
 10 top of the background state (*described below*). The vertical dimension of the model varied with time
 11 and was set using observed changes in mixed layer depth at the study site. The mixed layer interacted
 12 vertically with a bottom boundary condition through slow background exchange, $w_0(t)$, the velocity of
 13 which also varied over time.

14 To represent fine-scale biophysical interactions and the way they evolve over time, we branched
 15 the model from the background state to create new, discrete model environments. These branched

Model's physical framework: the simplest case ($tDist = 1$ day)

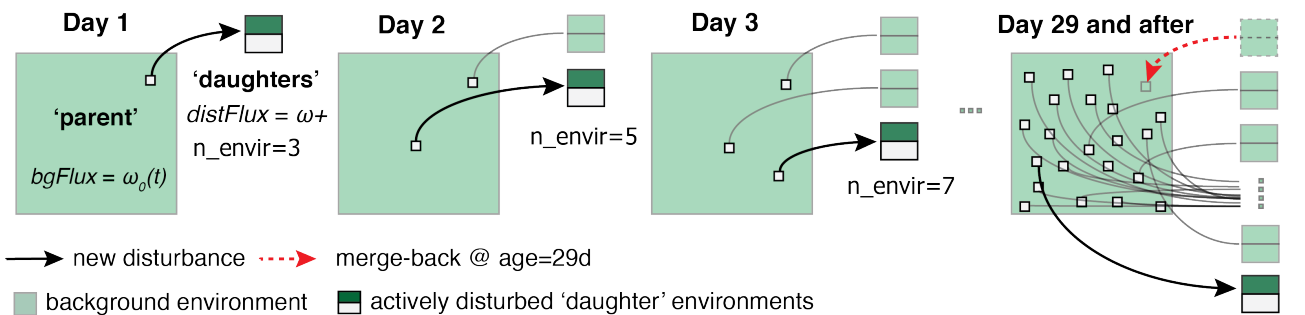


Figure 1. A schematic representation of the model's physical dynamics when run with short-lived, fine-scale subgrid frontal disturbances that last for 1-day. The evolution of subgrid environments over time is shown. Each day, a new pair of daughter environments is created by a frontal disturbance event and is isolated from the background environment. Light green denotes the background environment that experiences a small vertical velocity ($bgFlux = \omega_0(t)$) while dark green and white denote the actively disturbed daughter environments that experience an enhanced upwelling and downwelling velocity ($distFlux = \omega_+$), respectively. At the end of each disturbance period of length $tDist$ (here $tDist = 1$ day), this velocity is reset to the background level $\omega_0(t)$ in the disturbed daughter environments (light green). These daughters remain isolated from the background environment but connected with each other through diffusive exchange for a total of 28 days. Starting on Day 29, the oldest pair of the daughter environments (age = 29 days) is merged back to the background environment while a new pair is created at the same time. This allows the model to run with always 57 subgrid environments (1 background and 28 pairs of daughters) over the simulation period. Mass is conserved using an accounting term that tracks the fractional area of each daughter environment (see Eq. 1 below).

16 environments simulated the biogeochemical and ecological responses to a fine-scale frontal disturbance.
17 Specifically, we represented each fine-scale disturbance with a pair of new “daughter” environments,
18 which were branched from the background environment. The two daughters were horizontally
19 connected to each other by advection and diffusion during active disturbance, with one experiencing
20 an enhanced upwelling velocity of magnitude w_+ that injected nutrient-rich water from the deep
21 boundary layer, and the other experiencing an enhanced downwelling velocity of the same magnitude
22 that subducted organic-matter-enriched water from the surface. This simplification of an equal
23 magnitude of upwelling and downwelling velocity represents an idealization of the frontal structures
24 observed in high-resolution idealized models and regional ocean model simulations which are often
25 imbalanced (Mahadevan and Tandon 2006; Levy et al., 2012a, McWilliams, 2016, Nagai et al., 2015).
26 Exchanges between each pair of daughter environments were parameterized assuming a horizontal
27 length scale of 5 km, chosen as a typical length scale for fine-scale frontal features. Sensitivity tests
28 demonstrated that the overall model dynamics were not impacted by the choice of this horizontal length
29 scale within a reasonable range (i.e., less than a few tens of kilometers).

30 Each daughter environment remained in the *disturbance state* (i.e., enhanced vertical velocities)
31 for a given duration, $tDist$. At the end of the disturbance period, the vertical velocities were reset to
32 the background level of $w_0(t)$. Since the biogeochemical impact of the disturbance continued after this
33 period, the two daughters remained isolated from the background environment, though still connected
34 to each other through diffusive exchange, until key ecosystem properties converged to the background
35 state. Tests indicated that, for a reasonable range of values for $tDist$ (1 – 7 days) and w_+ (5 – 40 m day⁻¹),
36 28 days was sufficient time to capture the full evolution of the ecological and biogeochemical
37 response to the disturbance. Overall, this framework allowed for a systematic assessment of the impact

38 of fine-scale frontal disturbance across a range of intensities (different values of w_+) and durations
39 (different values of $tDist$) over a changing background state.

40 In order to meaningfully compare model runs with fine-scale disturbances of varying durations
41 and intensities, we added an accounting term to track the fractional contribution of each daughter
42 environment to the total model domain. At any point in time (t), the fractional model area actively
43 disturbed by fine-scale fronts can be defined as $\chi(t) = \Sigma(\text{fractional areas of actively disturbed daughters})$.
44 This includes daughter environments created both by new disturbances and by previous disturbances
45 initialized over the past $tDist$ period and thus still active at time point t . The $\chi(t)$ accounting term
46 allowed us to compare runs with the same spatially averaged vertical velocity into the mixed layer
47 $\bar{w}(t)$ but with different dynamics within the model domain, where:

$$48 \quad \bar{w}(t) = (1 - \chi(t))w_0(t) + \chi(t)w_+ \quad (1)$$

49 Specifically, using this framework, we can isolate the impact of changing the intensity (w_+) or duration
50 ($tDist$) of fine-scale disturbances on the spatially averaged ecological and biogeochemical model
51 properties by keeping all else constant. For example, two simulations with $w_+ = 5 \text{ m day}^{-1}$ and $w_+ = 40$
52 m day^{-1} could be compared either by assuming the w_0 remained constant and altering the accounting
53 term χ by solving Eq. 1, or by holding χ constant and altering w_0 . In this study, we chose the latter.
54 The accounting term does not impact the dynamics within the daughter environments, but simply
55 provides a standardized way to assess the spatially averaged impact of different disturbance types.

56 Tracking the fractional contribution of the daughter environments also allowed us to streamline
57 our model simulations. Rather than running thousands of individual simulations to test the impact of
58 a single type (same intensity and duration) of fine-scale front for each day over a 12-year period, we
59 were able to run a single model simulation as follows. Each day, we branched the model to simulate a
60 new physical disturbance event as described above (Fig. 1). After 28 days, the biogeochemical and

61 ecological state variables for the daughters being tracked in isolation had converged to the background
62 state (i.e., there was no longer biogeochemical or ecological memory of the disturbance in the daughter
63 environments). Thus, these environments were merged back into the background environment. The χ
64 accounting term allowed us to branch and merge subgrid environments while conserving mass. Overall,
65 this framework allowed the model to run continuously with 57 subgrid environments (1 background
66 and 28 pairs of daughters) over the entire simulation period. These runs are hereafter referred to as the
67 Heterogeneous Environment (HE) simulations (Fig. 1 & Eq. 1). We also conducted a set of model
68 simulations where $\chi(t)$ was set to zero. This configuration resulted in model dynamics analogous to a
69 traditional box model in which the entire model area responded homogeneously to the same boundary
70 condition and same average vertical velocity of magnitude $\bar{w}(t)$. These runs are hereafter referred to
71 as the Average Environment (AE) simulations.

72

73 2.2 Ecological model description

74 Biogeochemical and ecological dynamics were simulated in the background environment and each of
75 the daughter environments using a Nutrient, Phytoplankton, Zooplankton and Detrital (NPZD) model.
76 The model was adapted from Doney et al. (1996) and Moore et al. (2004, 2013) and tracked dissolved
77 nutrients (nitrate and ammonium), three phytoplankton functional groups (large phytoplankton such as
78 diatoms, small phytoplankton such as *Prochlorococcus*, and diazotrophs such as *Trichodesmium*),
79 zooplankton grazers, particulate organic carbon (POC), and dissolved organic carbon (DOC). The
80 evolution of these variables for the background environment j over time is calculated as:

$$81 \quad \frac{\partial Nit_j}{\partial t} = \frac{\partial}{\partial z} (w_0 Nit_b) - \frac{\partial}{\partial z} (w_0 Nit_j) - uptake_j \quad (1)$$

$$82 \quad \frac{\partial Amm_j}{\partial t} = \frac{\partial}{\partial z} (w_0 Amm_b) - \frac{\partial}{\partial z} (w_0 Amm_j) + S_{Amm(j)} - uptake_j \quad (2)$$

$$84 \quad \frac{\partial P_{i,j}}{\partial t} = \frac{\partial}{\partial z} (w_0 P_{i,b}) - \frac{\partial}{\partial z} (w_0 P_{i,j}) + \mu_{max(i)} \gamma_{i,j}^T \gamma_{i,j}^I \gamma_{i,j}^N P_{i,j} - mort P_{i,j} - g_i \frac{P_{i,j}}{P_{i,j} + k_{grz(i)}} Z_j \quad (3)$$

85
86
87
$$\frac{\partial Z_j}{\partial t} = \frac{\partial}{\partial z}(w_0 Z_b) - \frac{\partial}{\partial z}(w_0 Z_j) + \sum_i f_{g_zoo(i)} graze_{i,j} - mort Z_j \quad (4)$$

88
$$\frac{\partial POC_j}{\partial t} = \frac{\partial}{\partial z}(w_0 POC_b) - \frac{\partial}{\partial z}(w_0 POC_j) + S_{POC(j)} - remin_{POC(j)} - export_j \quad (5)$$

89
$$\frac{\partial DOC_j}{\partial t} = \frac{\partial}{\partial z}(w_0 DOC_b) - \frac{\partial}{\partial z}(w_0 DOC_j) + S_{DOC(j)} - remin_{DOC(j)} \quad (6)$$

90 where the first two terms on the right-hand side of equations 1-6 represent the advective vertical exchange
91 of material with the bottom layer denoted with “*b*”. w_0 is the advective vertical exchange with the bottom
92 boundary layer ($P_{i,b}$, here set to 0.1 mg C m^{-3}). It was assumed that the vertical flux w_0 into the model
93 domain was matched by a corresponding flux (either horizontal or vertical) out of the model domain.
94 *Nit* and *Amm* are consumed by phytoplankton (*uptake*). $S_{Amm(j)}$ are the sources of ammonium to the
95 background environment *j* including POC remineralization, DOC remineralization, phytoplankton and
96 zooplankton respiration, and sloppy grazing. $S_{POC(j)}$ are the sources of POC to the background environment
97 *j* including phytoplankton mortality and aggregation, zooplankton mortality, and sloppy grazing. $S_{DOC(j)}$
98 are the sources of DOC to the background environment *j* including respiration and sloppy grazing. For the
99 daughter environments, equations 1-6 were modified to include advective and diffusive exchange between
100 the upwelling (*j*⁺) and downwelling (*j*⁻) environments (see equations below). POC was exported from the
101 surface ocean through aggregation and sinking. Temperature was solved for prognostically as a
102 function of surface short-wave radiative warming, long-wave radiative cooling, wind driven surface
103 cooling, and mixing with a cold deep boundary layer following Marshall and Plumb (2008).

104 Three phytoplankton functional types (PFTs) are included: an ‘opportunist’ large-phytoplankton
105 (e.g. diatoms), a ‘gleaner’ pico-phytoplankton (e.g. *Prochlorococcus* and *Synechococcus*), and a N₂-fixing
106 phytoplankton group such as *Trichodesmium spp.* Phytoplankton growth for each group (μ_{max}) is limited
107 by temperature ($\gamma_{i,j}^T$), light ($\gamma_{i,j}^I$), and nitrogen ($\gamma_{i,j}^N$). Nutrient limitation was imposed through the half
108 saturation constants (k_n for nitrate and k_{am} for ammonium) following Geider et al. (1998). Temperature

109 limitation on growth was modified to follow the formulation of Follows *et al.* (2007). Photosynthetically
 110 active radiation is calculated from incoming shortwave radiation and model chlorophyll concentrations
 111 (Morel and Maritorena, 2001). Phytoplankton loss is due to non-grazing mortality ($mortP_{i,j}$), which is a
 112 function of temperature and cell density, and grazing mortality ($graze_{i,j}$), which is modeled using a Holling
 113 II relationship (Holling, 1965):

$$114 \quad graze_{i,j} = g_i \frac{P_{i,j}}{P_{i,j} + k_{grz(i)}} T_{func} Z_j \quad (7)$$

115 where g_i is the phytoplankton specific maximum grazing rate, $k_{grz(i)}$ is the phytoplankton specific grazing
 116 coefficient, and T_{func} is a Q₁₀ temperature function. Zooplankton growth is prey dependent with a larger
 117 fraction of POC production (sloppy grazing) resulting when large-phytoplankton are grazed. Zooplankton
 118 mortality is a function of temperature and population size. Remineralization converts POC and DOC back
 119 to inorganic carbon and nitrogen. Key parameters used in the model are provided in Appendix A.

120

121 For the daughter environments, Eqs. 1-6 were modified to include advective and diffusive
 122 exchange between the upwelling ($j+$) and downwelling ($j-$) daughter environments. Specifically,
 123 during active disturbance, the evolution of phytoplankton biomass (as an example) in each environment
 124 was calculated as:

$$125 \quad \frac{\partial P_{i,j+}}{\partial t} = \frac{\partial}{\partial z} (w_+ P_{i,b}) - \frac{\partial}{\partial x} (u P_{i,j+}) + \frac{\partial}{\partial x^2} (K \Delta P_{i,j*}) + \mu_{max(i)} \gamma_{i,j+}^T \gamma_{i,j+}^I \gamma_{i,j+}^N P_{i,j+} - mort P_{i,j+} -$$

$$126 \quad g_i \frac{P_{i,j+}}{P_{i,j+} + k_{grz(i)}} Z_{j+} \quad (8)$$

$$127 \quad \frac{\partial P_{i,j-}}{\partial t} = - \frac{\partial}{\partial z} (w_+ P_{i,j-}) + \frac{\partial}{\partial x} (u P_{i,j+}) - \frac{\partial}{\partial x^2} (K \Delta P_{i,j*}) + \mu_{max(i)} \gamma_{i,j-}^T \gamma_{i,j-}^I \gamma_{i,j-}^N P_{i,j-} - mort P_{i,j-} -$$

$$128 \quad g_i \frac{P_{i,j-}}{P_{i,j-} + k_{grz(i)}} Z_{j-} \quad (9)$$

129 where u is the advective horizontal transport between daughter environments and equal to $w_+ \frac{\partial x}{\partial z}$ for
 130 mass balance. K (1.0 m s⁻¹) is the diffusive exchange between each pair of the daughters acting on the

131 concentration gradient between the upwelling and downwelling environments ($\Delta P_{i,j*}$) over length scale
 132 dx . After the disturbance interval ($tDist$), the vertical exchange in the daughter environments returned
 133 to the background state and the phytoplankton dynamics were calculated as (akin to Eqs. 1-6) but
 134 retaining diffusive exchange between daughter environments (using phytoplankton as an example):

$$135 \quad \frac{\partial P_{i,j+}}{\partial t} = \frac{\partial}{\partial z} (w_0 P_{i,b}) - \frac{\partial}{\partial z} (w_0 P_{i,j+}) + \frac{\partial}{\partial x^2} (K \Delta P_{i,j*}) + \mu_{max(i)} \gamma_{i,j+}^T \gamma_{i,j+}^I \gamma_{i,j+}^N P_{i,j+} - mort P_{i,j+} -$$

$$136 \quad g_i \frac{P_{i,j+}}{P_{i,j+} + k_{grz(i)}} Z_{j+} \quad (10)$$

$$137 \quad \frac{\partial P_{i,j-}}{\partial t} = \frac{\partial}{\partial z} (w_0 P_{i,b}) - \frac{\partial}{\partial z} (w_0 P_{i,j-}) - \frac{\partial}{\partial x^2} (K \Delta P_{i,j*}) + \mu_{max(i)} \gamma_{i,j-}^T \gamma_{i,j-}^I \gamma_{i,j-}^N P_{i,j-} - mort P_{i,j-} -$$

$$138 \quad g_i \frac{P_{i,j-}}{P_{i,j-} + k_{grz(i)}} Z_{j-} \quad (11)$$

139

140 **Model configuration and simulations**

141 The model was run for the Hawaiian Ocean Time-series (HOT) site located at 22°45'N,
 142 158°00'W in the North Pacific Subtropical Gyre from 2003-2014. The horizontal dimension of the
 143 entire model domain was defined as a 5° × 5° region centered at the HOT site. Observed monthly
 144 mixed layer depth values averaged over the model domain (from [Argo Mixed Layers](#), accessed on
 145 01/27/2016) were used to set the model's varying vertical dimension. This product was calculated
 146 from Argo float profiles using a hybrid approach based on a traditional threshold and gradient method
 147 (Holte and Talley, 2009; Holte et al., 2017). The model was forced with photosynthetically active
 148 radiation (PAR; [OB.DAAC MODIS-Aqua L3](#), accessed on 02/12/2016), air temperature, and wind
 149 speed at 10 m above the sea surface (NCEP/NCAR Reanalysis 1 accessed on 01/30/2016). The bottom
 150 boundary conditions were defined using observed temperature and nitrate values at the HOT site
 151 averaged between the bottom of the mixed layer and the first depth at which density was 2 kg m⁻³
 152 greater than that averaged over the mixed layer ([HOT-DOGS](#), accessed on 12/05/2015). All monthly

153 boundary conditions were interpolated into pseudo-daily values. Hourly PAR values were generated
154 from pseudo-daily values following Stull (1988).

155 To realistically assess the spatially averaged impact of fine-scale frontal disturbances, the
156 dynamics of frontal disturbances were created using an estimate of the total fractional area being
157 actively disturbed by fine-scale frontal features (χ) calculated from MODIS-Aqua L2 Sea Surface
158 Temperature following Liu and Levine (2016). As daily SST images often contain large areas of
159 missing data potentially leading to erroneous χ estimates, monthly means of daily χ estimates were
160 computed and then interpolated to pseudo-daily values. Pseudo-daily χ values used in the model ranged
161 from 0.2 to 3.8% with a mean of 2.9%. For simulating the HOT site, a seasonally varying background
162 velocity $w_0(t)$ was used, ranging from 0.1 to 0.24 m day⁻¹, in order to account for the temporal
163 variability of mesoscale processes in the region that are important for vertical mixing in the upper ocean.
164 The magnitude of disturbance upwelling and downwelling velocity w_+ for these simulations was set at
165 20 m day⁻¹ to represent the typical condition at a fine-scale front (Mahadevan and Tandon, 2006).

166 The model was spun-up for two years using repeating forcing from Year 2003 to an
167 approximate steady-state, then numerically integrated for a total of 12 years between 2003 and 2014.
168 Key ecosystem parameters (Appendix A) were optimized using the Nelder-Mead Simplex Algorithm
169 (<https://www.mathworks.com/matlabcentral/fileexchange/69636-nelder-and-mead-simplex-algorithm>)
170 in MATLAB to minimize the model-observational differences in terms of the monthly climatologies
171 of mixed layer averaged temperature, nitrate concentration, and total primary production between 2003
172 and 2008. This 6-year period was only used for model optimization, while all model validations were
173 performed using model results between 2009 and 2014.

174

175 **Acknowledgements**

176 This study was supported by the National Science Foundation (OCE-RIG 1323319 and OCE
 177 1538525 awarded to N. Levine), NASA Earth and Space Science Fellowship (NNX14AK76H awarded
 178 to X. Liu), and University of Southern California.

179

180 Appendix A. Key ecosystem parameters used in the model. Parameters optimized for the HOT site
 181 are denoted with asterisks.

182

Parameters	Values
small phytoplankton maximum growth rate (day^{-1}), $\mu_{max(sm)}$	1.62*
large phytoplankton maximum growth rate (day^{-1}), $\mu_{max(lg)}$	2.60*
diazotroph maximum growth rate (day^{-1}), $\mu_{max(di)}$	0.78*
small phytoplankton nitrate uptake half-saturation coeff. (mmol m^{-3}), $k_{n(sm)}$	0.1*
large phytoplankton nitrate uptake half-saturation coeff. (mmol m^{-3}), $k_{n(lg)}$	0.5*
diazotroph nitrate uptake half-saturation coeff. (mmol m^{-3}), $k_{n(di)}$	2.0
small phytoplankton ammonium uptake half-saturation coeff. (mmol m^{-3}), $k_{am(sm)}$	0.015
large phytoplankton ammonium uptake half-saturation coeff. (mmol m^{-3}), $k_{am(lg)}$	0.04
diazotroph ammonium uptake half-saturation coeff. (mmol m^{-3}), $k_{am(di)}$	0.25
zooplankton maximum growth rate when grazing small phytoplankton (day^{-1}), $g_{(sm)}$	2.0*
zooplankton maximum growth rate when grazing large phytoplankton (day^{-1}), $g_{(lg)}$	2.2*
zooplankton maximum growth rate when grazing diazotrophs (day^{-1}), $g_{(di)}$	1.0
small phytoplankton maximum aggregation rate (day^{-1}), used to calculate $mort_{(sm)}$	0.3
large phytoplankton maximum aggregation rate (day^{-1}), used to calculate $mort_{(lg)}$	0.9
diazotroph non-grazing mortality (day^{-1}), $mort_{(di)}$	0.15
fraction of grazed matter added to zooplankton biomass when grazing small and large phytoplankton, $k_{grz(sm)}$ and $k_{grz(lg)}$	0.25
fraction of grazed matter added to zooplankton biomass when grazing diazotrophs, $k_{grz(di)}$	0.3
small phytoplankton optimal temperature for growth ($^{\circ}\text{C}$), used to calculate $\gamma_{(sm)}^T$	22.5
large phytoplankton optimal temperature for growth ($^{\circ}\text{C}$), used to calculate $\gamma_{(lg)}^T$	25
diazotroph phytoplankton optimal temperature for growth ($^{\circ}\text{C}$), used to calculate $\gamma_{(di)}^T$	27.5

183

References

- Doney, S. C., I. Lima, J. K. Moore, K. Lindsay, M. J. Behrenfeld, T. K. Westberry, N. Mahowald, D. M. Glover, T. Takahashi (2009), Skill metrics for confronting global upper ocean ecosystem-biogeochemistry models against field and remote sensing data. *J. Mar. Syst.*, 76, 95-112.
- Geider, R. J., H. L. MacIntyre, T. M. Kana (1998), A dynamic regulatory model of phytoplanktonic acclimation to light, nutrients, and temperature. *Limnology and Oceanography*, 43, 679-694.
- Holling, C.S., 1965. The Functional Response of Predators to Prey Density and its Role in Mimicry and Population Regulation. *Memoirs of the Entomological Society of Canada* 97, 5-60.
- Holte, J., J. Gilson, T. Talley, D. Roemmich (2010), Argo Mixed Layers, Scripps Institution of Oceanography/UCSD, <http://mixedlayer.ucsd.edu>, accessed on 2015/03/15.
- Holte, J., Talley, L.D., Gilson, J., Roemmich, D., 2017. An Argo mixed layer climatology and database. *Geophys. Res. Lett.* 44, 5618–5626. <https://doi.org/10.1002/2017GL073426>.
- Levy, M., R. Ferrari, P. J. S. Franks, A. P. Martin, and P. Riviere (2012a), Bringing physics to life at the submesoscale, *Geophys. Res. Lett.*, 39, L14602.
- Liu, X., and N. M. Levine (2016), Enhancement of phytoplankton chlorophyll by submesoscale frontal dynamics in the North Pacific Subtropical Gyre. *Geophys. Res. Lett.*, 43, 1651–1659.
- Mahadevan, A., and A. Tandon (2006), An analysis of mechanisms for submesoscale vertical motion at ocean fronts, *Ocean Model.*, 14, 241-256.
- McWilliams J. C. (2016), Submesoscale currents in the ocean. *Proc. R. Soc. A*, 472, 20160117.
- Moore, J. K., S. C. Doney, K. Lindsay (2004), Upper ocean ecosystem dynamics and iron cycling 798 in a global three-dimensional model. *Global Biogeochemical Cycles* 18, GB4028.
- Moore, J. K., K. Lindsay, S. C. Doney, M. C. Long, K. Misumi (2013), Marine ecosystem dynamics and biogeochemical cycling in the Community Earth System Model [CESM1(BGC)]: Comparison of the 1990s with the 2090s under the RCP4.5 and RCP8.5 scenarios. *J. Clim.*, 26, 9291-9312.
- Morel, A., Maritorena, S., 2001. Bio-optical properties of oceanic waters: A reappraisal. *Journal of Geophysical Research: Oceans* 106, 7163-7180.
- Nagai, T., Gruber, N., Frenzel, H., Lachkar, Z., McWilliams, J. C., and Plattner, G. K. (2015), Dominant role of eddies and filaments in the offshore transport of carbon and nutrients in the California Current System. *J. Geophys. Res. Oceans* 120, 5318– 5341.
- Stull, B. R. (1988), *An Introduction to Boundary Layer Meteorology*, Kluwer Academic Publishers, Dordrecht, the Netherlands.